

Exploring the small-scale magnetic fields of the solar analog KIC 8006161 using asteroseismology

GUIFANG LIN,^{1,2} YAN LI,^{1,2,3,4} JIE SU,^{1,2,4} TAO WU,^{1,2,3,4} AND YUETONG WANG^{1,2,3}

¹*Yunnan Observatories, Chinese Academy of Sciences, Kunming 650216, People's Republic of China*

²*International Center of Supernovae at the Yunnan Key Laboratory, Kunming 650216, People's Republic of China*

³*University of Chinese Academy of Sciences, Beijing 100049, People's Republic of China*

⁴*Center for Astronomical Mega-Science, Chinese Academy of Sciences, Beijing, 100012, People's Republic of China*

ABSTRACT

The magnetic field is a significant and universal physical phenomenon in modern astrophysics. Small-scale magnetic fields are very important in the stellar atmosphere. They are ubiquitous, and strongly couple with the acoustic waves. Therefore, their presence affects the properties of acoustic waves in the stellar outer layer. In the present work, under the assumption that the small-scale magnetic features are the cause of the asteroseismic surface term (the frequency-dependent frequency offset between stars and their models), we explore the strength of such fields in the solar analog KIC 8006161. By considering the effect of small-scale magnetic fields in the stellar photosphere, we use the observed oscillation frequencies to constrain the inner structures and surface small-scale magnetic fields of solar-like star KIC 8006161. To agree with the existing observations, such as oscillation frequencies, and their frequency separation ratios, the theoretical model requires a small-scale magnetic field to form a magnetic-arch splicing layer in the stellar outer atmosphere. The small-scale magnetic field strengths for KIC 8006161 obtained from best-fit model with $Y_{\text{init}} = 0.249 + 1.33Z_{\text{init}}$ and Y_{init} as a free parameter, are approximately 96 G and 89 G, respectively. The corresponding locations of the magnetic-arch splicing layer are about 522 km and 510 km, respectively.

Keywords: star:atmosphere — star:magnetic fields — star:oscillation — star: photosphere — magnetic fields —magnetohydrodynamics

1. INTRODUCTION

The small-scale magnetic fields in the quiet solar photosphere are a fundamental component of solar magnetism. They are ubiquitous on the solar surface, and store a substantial amount of magnetic energy (e.g. [Stenflo 1994](#); [Trujillo Bueno et al. 2004](#)). They may contribute to coronal heating and the acceleration of the stellar wind ([Schrijver et al. 1998](#); [Schrijver & Title 2003](#)). Comprehending the small-scale magnetic fields may help us to solve many of the key problems in solar and stellar physics.

Currently, an increasing amount of observational data with high spatial resolution and polarization sensitivity is used to investigate the small-scale magnetic fields of the solar photosphere. [Lites et al. \(1996\)](#) first discovered the isolated, small-scale horizontal magnetic fields using the observations from the Advanced Stokes Polarimeter. [Trujillo Bueno et al. \(2004\)](#) used observed Hanle depolarization and a three-dimensional radiative transfer model to indicate that there was an ubiquitous tangled magnetic field with a strength of approximately 130 G. Based on observations of the Solar Optical Telescope onboard the Hinode space observatory with very high spatial resolution, [Lites et al. \(2008\)](#) obtained a mean field strength of about 55 G for horizontal fields, and around 11 G for vertical magnetic fields. They found the vertical fields were concentrated in the intergranular lanes, while the horizontal fields were mostly located at the edges of the bright granules. [Jin & Wang \(2015\)](#) used the spectro-polarimeter observations on Hinode to analyze the cyclic variation of the inter-network horizontal fields. They found that the horizontal fields with about 87 G did not vary with solar activity. Many scholars have also used a amount of high-precision spectro-polarimetric data to probe horizontal fields in the quiet photosphere (i.e. [Danilovic et al. 2010](#); [Martínez González et al. 2016](#); [Lites et al. 2017](#)). Furthermore, [Morosin et al. \(2020\)](#) used a spatially-regularized weak-field approximation (WFA) method to derive the stratification of the magnetic field vector in plage regions.

In the numerical simulation, [Schaffenberger et al. \(2005, 2006\)](#) utilized the CO⁵BOLD code to carry out a three-dimensional magnetohydrodynamic simulations spanning from the convection zone to the chromosphere. They discovered a small-scale ‘magnetic canopy’ at an altitude of about 400 km. There was ‘magnetic void’ with a field strength below the canopy of less than 3 G. [Abbett \(2007\)](#) simulated the quiet sun from the upper convection zone to the lower corona. They found long, horizontal ribbons of magnetic flux threading through the low chromosphere. [Schüssler & Vögler \(2008\)](#) carried out the radiative MHD simulations of dynamo action driven by near-surface convection and got that horizontal fields predominated in the spectral lines observed by the Hinode spectro-polarimeter. The corresponding ratio of the horizontal and vertical fields was 4 to 6 which was consistent with the observed one ([Lites et al. 2008](#)). [Steiner et al. \(2008\)](#) found that the horizontal field strength reached a local maximum at approximately 500 km in the photosphere, where the horizontal fields were 2 or 5.6 times stronger than the vertical component depending on the initial state or boundary conditions. Very similar results were also reported by [Rempel \(2014\)](#).

The small-scale magnetic fields in the photosphere are coupled with the acoustic waves ([Rosenthal et al. 2002; Bogdan et al. 2003; Cally 2007](#)). The ratio between magnetic pressure and gas pressure, although initially small, exhibits an exponential increase with altitude. This would affect the wave propagation speed. [Li et al. \(2021\)](#) considered the effects of small-scale magnetic fields in the quiet solar photosphere on the frequencies of solar p-mode oscillation. They found the reflection of the solar p-mode at the magnetic-arch splicing layer. They got the solar small-scale magnetic field strength about 90 G and the corresponding location was at a height of about 630 km.

For solar-like stars, there is a convective envelope on the stellar surface, which is very similar to that of the sun. Although, the origin of small-scale magnetic fields is still debated. Based on the theory of fast dynamo and numerical simulations, the thermally-driven turbulent convection was indicated to be an effective source for small-scale magnetic fields ([Cattaneo 1999](#)). The convective envelope may make the small-scale magnetic fields widespread on the surface of solar-like stars. At present, the small-scale magnetic fields of the sun have been directly observed by the Hinode spectro-polarimeter. For solar-like stars at great distance, it is very difficult to directly observe the small-scale magnetic fields due to the spatial resolution. Because the small-scale magnetic fields are coupled with sound waves, this provides an opportunity to detect small-scale magnetic fields by asteroseismology. By utilizing only the high-precision oscillation frequencies obtained from the Kepler short-cadence data ([Lund et al. 2017](#)), we can use asteroseismology to constrain the stellar interior structure and the small-scale magnetic fields for solar-like stars.

Because the magnetic fields can result in shifts in the oscillation frequencies ([Gough & Thompson 1990](#)), asteroseismology can be used to detect magnetic fields by the shifts in the oscillation frequencies. [Li et al. \(2022\)](#) detected the asymmetries in the multiplets of 3 red giant stars observed by Kepler, and used the asteroseismology to measure magnetic fields in their cores. [Deheuvels et al. \(2023\)](#) also detected the strong magnetic fields in the cores of 11 red giant stars by the g-mode period spacing.

In this work, we assume that the near-surface effect for solar-like stars is caused by the influence of the small-scale magnetic fields in the photosphere. We employ a method proposed by [Li et al. \(2021\)](#) to explore the strength of such field in solar-like stars. We choose a solar analog KIC 8006161. KIC 8006161 (HD 173701) is a solar-like G dwarf with a ~ 7.4 yr activity cycle ([Karoff et al. 2018](#)). Using the latest version of the Asteroseismic Modeling Portal (AMP), [Creevey et al. \(2017\)](#) presented the basic parameters (i.e. mass, radius and age) of KIC 8006161, which were very similar to those of the sun except for a higher surface metallicity. In addition, using Kepler photometry, [Karoff et al. \(2018\)](#) obtained a mean rotation period of 27 days for KIC 8006161 which is also very similar to that of the sun. Due to the possibility of comparing the stellar parameters and interior structure of KIC 8006161 with those of the sun, KIC 8006161 is considered the ideal target for studying small-scale magnetic fields by asteroseismology. Considering the effects of small-scale magnetic fields in the photosphere, we use the observed p-mode frequencies to constrain the small-scale magnetic field strength for KIC 8006161. In §2, we present the stellar model with small-scale magnetic fields in the stellar photosphere. In §3, we will show the results of the model and present the magnetic field strength for KIC 8006161. At last, we’ll give our summaries.

2. STELLAR MODEL WITH SMALL-SCALE MAGNETIC FIELDS

We use the MESA evolutionary code with version r-10398 to construct stellar structure and evolutionary models (e.g. [Paxton et al. 2011, 2018](#)). The OPAL equation of state tables are taken from [Rogers & Nayfonov \(2002\)](#) and the OPAL opacity tables are obtained from [Iglesias & Rogers \(1996\)](#). For simplicity, we adopt the Eddington gray-atmosphere model as the stellar atmosphere model and use the GS98 ([Grevesse & Sauval 1998](#)) chemical composition. In the stellar structure and evolutionary models, we treat convection as the standard mixing length theory ([Böhm-Vitense 1958](#)), and

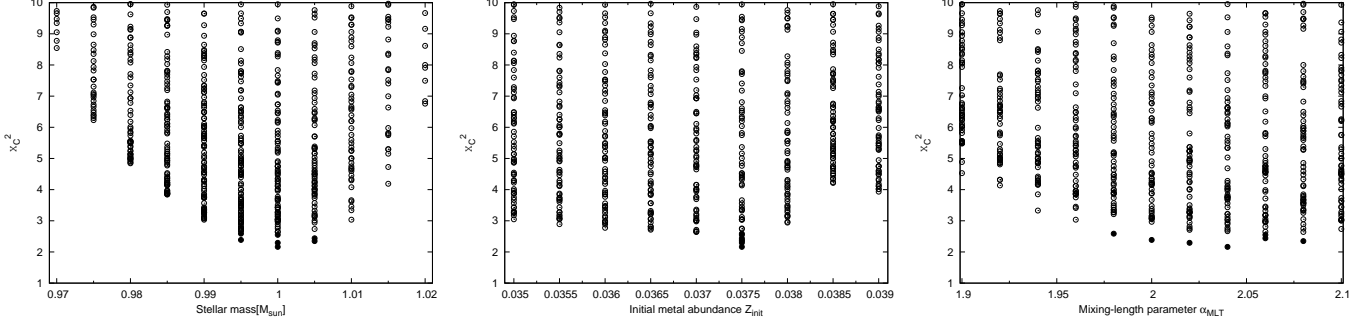


Figure 1. The distribution of χ_C^2 with stellar parameters. The panels from left to right represent the distribution of χ_C^2 with stellar mass, initial metal abundance Z_{init} , and mixing-length parameter α_{MLT} , respectively. The filled circles represent the results of models with $\chi_C^2 < 2.6$.

do not consider convective overshooting. We use the default parameters to include the element diffusion. In addition, we also take into account the radiative diffusivity (Morel & Thévenin 2002). In order to get the theoretical p-mode oscillation frequencies which are compared with the observed ones, we use the "adipls" package (Christensen-Dalsgaard 2008) in MESA to solve the adiabatic oscillation equations. In the evolutionary models, in order to get more detailed information about stellar structure, we set the outer boundary of the stellar atmosphere with a very low density 10^{-10} and adjust the mesh with at least 8000 cells.

Li et al. (2021) modeled the effect of small-scale magnetic fields on solar oscillation frequencies by adding magnetic pressure in the solar atmosphere model. Based on their work, we construct the stellar interior structure of the solar analog KIC 8006161 with the effects of magnetic fields in the photosphere. In the Eddington gray-atmosphere model, we use the unified $T - \tau$ relation (Li et al. 2021):

$$T^4 = \frac{3}{4} T_{\text{eff}}^4 [\tau + q(\tau)] \quad (1)$$

In the above equation, an additional term in the Hopf-like function $q(\tau)$ is added: $q(\tau) = q_{\text{ori}}(\tau) + a \exp(-b\sqrt{\tau})$, in which the second term mimics the effect of magnetic fields. In the Eddington gray-atmosphere model, q_{ori} is $2/3$. Parameters a and b represent the magnetic field strength and the location of the magnetic-arch splicing layer, respectively. In Eq. (1), the additional term indicates an increase in temperature in the photosphere. The part where the radiative pressure increases represents the effect of the magnetic pressure. In the stellar photosphere, as the magnetic pressure increases, the gas pressure decreases which leads to a rapid decrease in density. The sound speed may increase rapidly. When the acoustic waves propagate to the magnetic-arch splicing layer, they will be reflected or transmitted. For the reflected standing waves, $P' = 0$ is adopted as the surface mechanical boundary condition. For more details, please refer to Li et al. (2021).

By using the Kepler short-cadence data, Lund et al. (2017) extracted 54 oscillation frequencies for KIC 8006161 and presented the corresponding frequency ratios. The errors of the observed frequencies and frequency ratios are also presented in Lund et al. (2017). Using the Kepler observed 54 modes with angular degree $l = 0 \sim 3$, we construct the stellar interior structure for KIC 8006161 with magnetic fields in the photosphere.

Based on the spectroscopic observations, we set wide ranges of initial input parameters for the theoretical models: $M \sim 0.96 - 1.03 M_{\odot}$ with a step of $0.005 M_{\odot}$, $Z_{\text{init}} \sim 0.03 - 0.04$ with a step of 0.0005 , $\alpha \sim 1.7 - 2.32$ with a step of 0.04 . We use the relation of $Y_{\text{init}} = 0.249 + 1.33 Z_{\text{init}}$ (Li et al. 2018) to calculate the initial helium abundance.

3. CALCULATIONS AND RESULTS

3.1. Theoretical results

In our work, based on Li et al. (2021), we introduce the magnetic pressure in the stellar photosphere. Due to the coupling between the magnetic fields and the acoustic waves, the magnetic field strength and the location of the magnetic-arch splicing layer in the photosphere must be very important for stellar models.

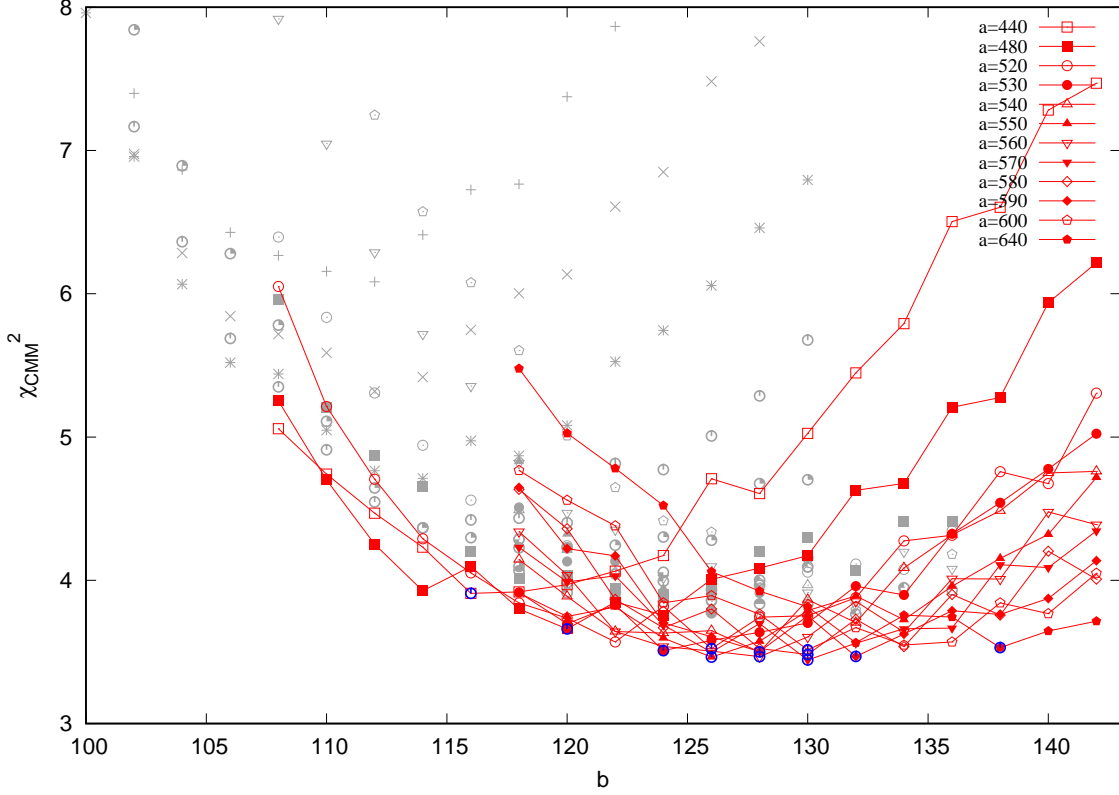


Figure 2. The distribution of χ_{CMM}^2 with the parameters a and b of magnetic fields. The grey points represent the results obtained from the model with initial fundamental parameters, while the red lines correspond to the results derived from the χ^2 -minimization model with $M = 1.0M_{\odot}$, $Z_{\text{init}} = 0.032$, $\alpha = 2.12$. The points sharing the same type indicate the results with an identical parameter a .

In order to reduce the amount of calculations, we use an iterative computation method to get self-consistent magnetic parameters a and b . The small-scale magnetic fields in the stellar photosphere only influent the stellar surface structure. For solar-like stars, [Roxburgh & Vorontsov \(2003\)](#) found that the ratios r_{ij} of small to large-frequency separations are only determined by the stellar interior structure. The ratio of small to large-frequency separations r_{ij} are defined as follows ([Roxburgh & Vorontsov 2003](#)):

$$r_{01}(n) = \frac{\delta\nu_{01}(n)}{\Delta\nu_{l=1}(n)}, r_{02}(n) = \frac{\delta\nu_{02}(n)}{\Delta\nu_{l=1}(n)} \quad (2)$$

and

$$r_{10}(n) = \frac{\delta\nu_{10}(n)}{\Delta\nu_{l=0}(n+1)} \quad (3)$$

in which

$$\Delta\nu_l(n) = \nu_{n,l} - \nu_{n-1,l} \quad (4)$$

$$\delta\nu_{02}(n) = \nu_{n,0} - \nu_{n-1,2} \quad (5)$$

$$\delta\nu_{01}(n) = \frac{1}{8}(\nu_{n-1,0} - 4\nu_{n-1,1} + 6\nu_{n,0} - 4\nu_{n,1} + \nu_{n+1,0}) \quad (6)$$

and

$$\delta\nu_{10}(n) = -\frac{1}{8}(\nu_{n-1,1} - 4\nu_{n,0} + 6\nu_{n,1} - 4\nu_{n+1,0} + \nu_{n+1,1}). \quad (7)$$

This means that if the stellar interior structure remains unchanged, changing only the surface structure will not change the ratios r_{ij} . For KIC 8006161, we use the observed frequency ratios r_{ij} and the spectral parameters (i.e. T_{eff} ,

$\log g$, $[\text{Fe}/\text{H}]$) to constrain the stellar initial fundamental parameters. We use a χ_C^2 minimization model as an initial one through a comparison of models with observations:

$$\chi_C^2 = \sum_{i=1}^4 \left(\frac{C_i^{\text{theo}} - C_i^{\text{obs}}}{\sigma_{C_i^{\text{obs}}}} \right)^2 \quad (8)$$

in which $C = (r_{\text{ij}}, T_{\text{eff}}, \log g, [\text{Fe}/\text{H}])$. C_i^{theo} is the theoretical values and C_i^{obs} is the observational ones. $\sigma_{C_i^{\text{obs}}}$ is the errors of the observations. The distribution of χ_C^2 with the parameters is shown in Fig. 1. We choose the model with the minimum χ_C^2 as the initial fundamental model: $M = 1.0M_{\odot}$, $Z_{\text{init}} = 0.0375$, $\alpha = 2.04$.

Using the initial fundamental parameters, we preliminarily determine the values of a and b . Then, we calculate the stellar structure and evolution of the models with these values, and get the χ^2 -minimization model. In this model, it is defined as (i.e. Eggenberger et al. 2004, Wu & Li 2016)

$$\chi_{\text{CMM}}^2 = \frac{1}{N} \sum_{i=1}^N \left(\frac{\nu_i^{\text{obs}} - \nu_i^{\text{theo}}}{\sigma_{\nu_i^{\text{obs}}}} \right)^2 \quad (9)$$

in which ν_i^{obs} and ν_i^{theo} are observed frequencies and theoretical ones, respectively. $\sigma_{\nu_i^{\text{obs}}}$ is the errors of the observed frequencies. N is the total observed frequencies number. When the initial input fundamental parameters are the same as those of the χ^2 -minimization model, the values of a and b are adopted as the optimal ones. If they are different, the aforementioned process must be iterated until the condition is satisfied. We also explore the utilization of diverse initial fundamental parameters. After iterative computation, the optimal values of parameters a and b exhibit remarkable proximity.

According to the work of Wu & Li (2016), there is one χ^2 -minimization model (CMM) for an evolutionary track with a set of fundamental parameters. The optimal magnetic parameters a and b for KIC 8006161 are 570 and 130, respectively, after two iterations. Fig. 2 presents the distribution of χ_{CMM}^2 with the parameters a and b of magnetic fields. The grey points are the distribution of χ_{CMM}^2 for the model with initial fundamental parameters. The red points are those obtained from the χ -minimization model with $M = 1.0M_{\odot}$, $Z_{\text{init}} = 0.032$ and $\alpha = 2.12$ after 2 iterations. It can be seen that when the value of a is fixed and b increases, the value of χ_{CMM}^2 firstly decreases, then increases. The positions with lowest χ_{CMM}^2 for different a are marked with blue dots. As the parameter a increases, χ_{CMM}^2 gradually decreases until it reaches a minimum at $a = 570$, after which it gradually increases. Using the iterative calculations method described above, we get the fundamental parameters of the model with the minimum $\chi_{\text{CMM}}^2 = 3.444$: $M = 1.0M_{\odot}$, $Z_{\text{init}} = 0.032$, $\alpha = 2.12$. We use the models with $\chi_{\text{CMM}}^2 < 4.0$ (i.e. within twice the error bar of observed frequencies) as better candidate models, and their fundamental parameters are listed in Table 1. Among these candidate models, we select model M48 with a minimum $\chi_{\text{CMM}}^2 = 3.44$ as the best-fit model. We use the notation x_{-dx}^{+dx} to describe the values of stellar parameters, where x represents the value of the best-fit model, and dx represents the maximum deviation between the candidate models and the best-fit model. The corresponding stellar parameters are listed in Table 2.

Table 1. The fundamental parameters for the better candidate models with the parameters $a=570$, $b=130$ and $\chi_{\text{CMM}}^2 < 4.0$.

No.	$M[M_{\odot}]$	Z_{init}	α_{MLT}	$R[R_{\odot}]$	T_{eff}	$L[L_{\odot}]$	$\log g$	X_{H}	$t_{\text{age}}[\text{Gyr}]$	$R_{\text{CZ}}[R_{\odot}]$	$[\text{Fe}/\text{H}]$	X_s	Y_s	χ_{CMM}^2
1	0.990	0.0370	2.02	0.931	5475	0.700	4.496	0.375	4.830	0.633	0.339	0.689	0.276	3.895
2	0.995	0.0315	2.10	0.932	5583	0.758	4.497	0.378	4.685	0.639	0.261	0.701	0.269	3.940
3	0.995	0.0315	2.12	0.932	5591	0.763	4.497	0.372	4.762	0.638	0.261	0.702	0.269	3.867
4	0.995	0.0320	2.10	0.932	5576	0.755	4.497	0.377	4.700	0.638	0.269	0.700	0.270	3.814
5	0.995	0.0320	2.12	0.932	5585	0.760	4.497	0.371	4.776	0.637	0.268	0.700	0.270	3.820
6	0.995	0.0325	2.08	0.932	5562	0.747	4.497	0.381	4.641	0.638	0.277	0.699	0.271	3.881
7	0.995	0.0325	2.10	0.932	5571	0.752	4.497	0.375	4.720	0.637	0.276	0.699	0.271	3.883
8	0.995	0.0325	2.12	0.932	5579	0.757	4.497	0.370	4.795	0.637	0.276	0.699	0.270	3.886
9	0.995	0.0330	2.08	0.932	5557	0.745	4.497	0.379	4.662	0.637	0.284	0.698	0.271	3.973
10	0.995	0.0330	2.10	0.932	5565	0.749	4.497	0.374	4.740	0.637	0.284	0.698	0.271	3.953

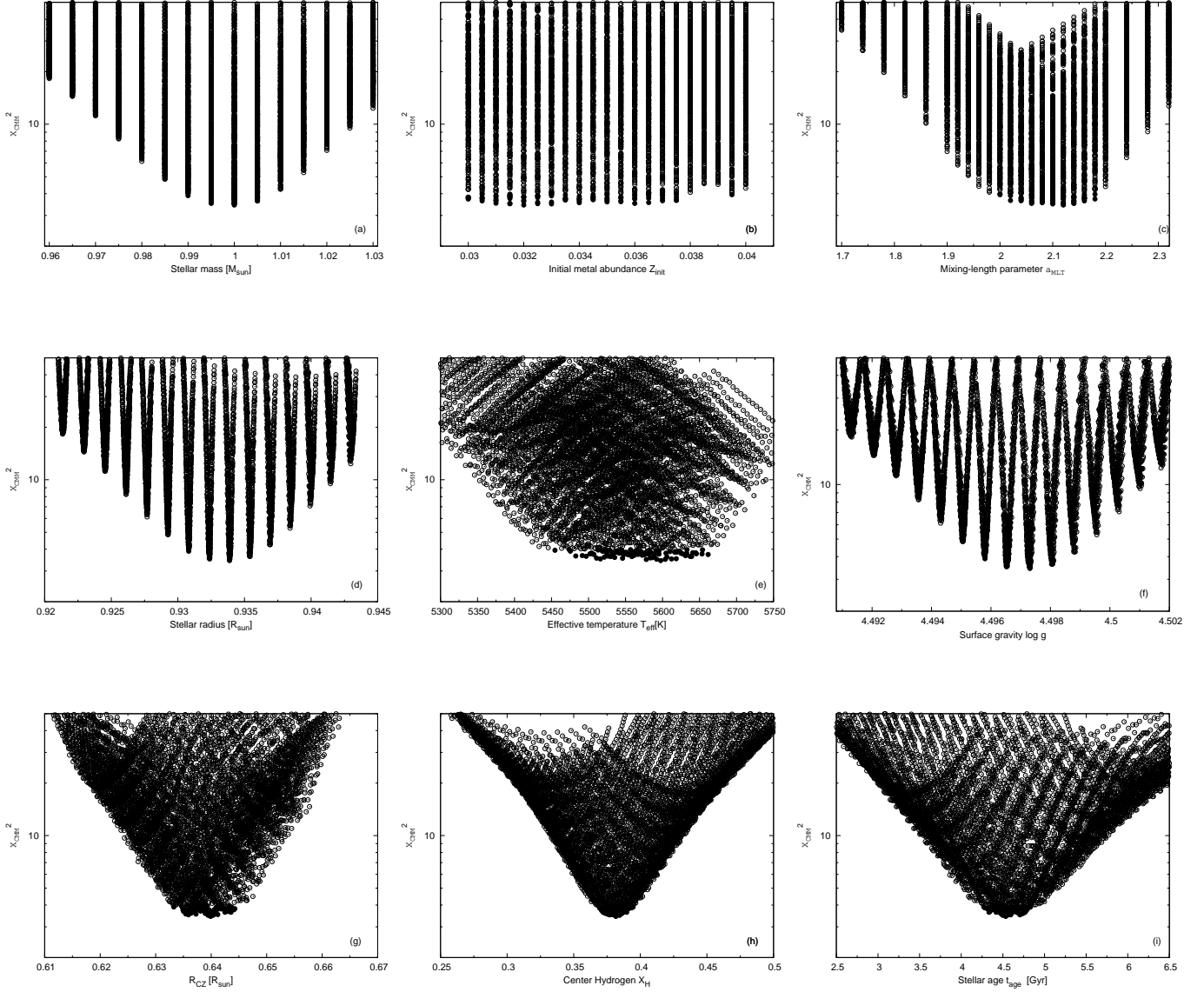


Figure 3. The distribution of χ_{CMM}^2 with stellar parameters when fixing the magnetic parameters as $a = 570$ and $b = 130$ and setting the initial helium abundance as $Y_{\text{init}} = 0.249 + 1.33Z_{\text{init}}$. The panels (a)-(i) represent the distribution of χ_{CMM}^2 with stellar mass, initial metal abundance Z_{init} , mixing-length parameter α_{MLT} , stellar radius, effective temperature T_{eff} , surface gravity $\log g$, location of convection zone bottom R_{CZ} , center hydrogen X_{H} , and stellar age t_{age} , respectively. The filled circles represent the results of better candidate models in Table 1.

No.	$M[M_{\odot}]$	Z_{init}	α_{MLT}	$R[R_{\odot}]$	T_{eff}	$L[L_{\odot}]$	$\log g$	X_{H}	$t_{\text{age}}[\text{Gyr}]$	$R_{\text{CZ}}[R_{\odot}]$	$[\text{Fe}/\text{H}]$	X_{s}	Y_{s}	χ_{CMM}^2
11	0.995	0.0335	2.08	0.932	5551	0.742	4.497	0.378	4.682	0.637	0.291	0.697	0.272	3.760
12	0.995	0.0335	2.10	0.932	5560	0.746	4.497	0.372	4.760	0.637	0.291	0.697	0.272	3.675
13	0.995	0.0340	2.06	0.932	5537	0.734	4.497	0.382	4.622	0.638	0.299	0.695	0.273	3.855
14	0.995	0.0340	2.08	0.932	5546	0.739	4.497	0.377	4.703	0.637	0.299	0.695	0.273	3.550
15	0.995	0.0340	2.10	0.932	5555	0.743	4.497	0.371	4.782	0.637	0.298	0.696	0.272	3.715
16	0.995	0.0345	2.06	0.932	5532	0.731	4.497	0.381	4.642	0.637	0.306	0.694	0.274	3.819
17	0.995	0.0345	2.08	0.932	5541	0.736	4.497	0.375	4.724	0.636	0.305	0.694	0.273	3.812
18	0.995	0.0345	2.10	0.932	5549	0.741	4.497	0.370	4.803	0.636	0.305	0.695	0.273	3.836

No.	$M[M_{\odot}]$	Z_{init}	α_{MLT}	$R[R_{\odot}]$	T_{eff}	$L[L_{\odot}]$	$\log g$	X_{H}	$t_{\text{age}}[\text{Gyr}]$	$R_{\text{CZ}}[R_{\odot}]$	$[\text{Fe}/\text{H}]$	X_{s}	Y_{s}	χ_{CMM}^2
19	0.995	0.0350	2.06	0.932	5527	0.728	4.497	0.380	4.664	0.637	0.313	0.693	0.274	3.652
20	0.995	0.0350	2.08	0.932	5535	0.733	4.497	0.374	4.744	0.636	0.312	0.693	0.274	3.586
21	0.995	0.0350	2.10	0.932	5544	0.738	4.496	0.368	4.823	0.636	0.312	0.694	0.274	3.977
22	0.995	0.0355	2.06	0.932	5521	0.726	4.497	0.378	4.684	0.636	0.320	0.692	0.275	3.599
23	0.995	0.0355	2.08	0.932	5530	0.730	4.497	0.372	4.766	0.636	0.319	0.692	0.275	3.630
24	0.995	0.0360	2.04	0.932	5507	0.718	4.497	0.382	4.621	0.637	0.327	0.691	0.276	3.730
25	0.995	0.0360	2.06	0.932	5516	0.723	4.497	0.377	4.704	0.636	0.327	0.691	0.275	3.519
26	0.995	0.0360	2.08	0.932	5525	0.728	4.496	0.371	4.787	0.635	0.326	0.691	0.275	3.766
27	0.995	0.0365	2.04	0.932	5502	0.716	4.497	0.381	4.643	0.636	0.334	0.689	0.276	3.765
28	0.995	0.0365	2.06	0.932	5511	0.720	4.497	0.375	4.726	0.635	0.333	0.690	0.276	3.557
29	0.995	0.0365	2.08	0.932	5519	0.725	4.496	0.369	4.807	0.635	0.333	0.690	0.276	3.888
30	0.995	0.0370	2.04	0.932	5497	0.713	4.497	0.379	4.663	0.636	0.340	0.688	0.277	3.642
31	0.995	0.0370	2.06	0.932	5506	0.718	4.496	0.374	4.747	0.635	0.340	0.689	0.277	3.760
32	0.995	0.0375	2.00	0.932	5474	0.701	4.497	0.390	4.510	0.636	0.348	0.687	0.278	3.984
33	0.995	0.0375	2.02	0.932	5483	0.706	4.497	0.384	4.598	0.636	0.348	0.687	0.278	3.655
34	0.995	0.0375	2.04	0.932	5492	0.710	4.497	0.378	4.683	0.635	0.347	0.687	0.278	3.675
35	0.995	0.0395	2.00	0.932	5455	0.691	4.497	0.380	4.670	0.635	0.373	0.683	0.280	3.945
36	1.000	0.0300	2.14	0.934	5632	0.789	4.497	0.380	4.551	0.642	0.238	0.704	0.268	3.801
37	1.000	0.0300	2.16	0.934	5641	0.793	4.497	0.374	4.625	0.641	0.238	0.705	0.267	3.821
38	1.000	0.0305	2.14	0.934	5625	0.784	4.497	0.379	4.568	0.642	0.246	0.703	0.268	3.805
39	1.000	0.0305	2.16	0.934	5633	0.789	4.497	0.373	4.641	0.641	0.246	0.704	0.268	3.734
40	1.000	0.0310	2.12	0.934	5610	0.776	4.497	0.384	4.507	0.641	0.255	0.702	0.269	3.874
41	1.000	0.0310	2.14	0.934	5618	0.781	4.497	0.378	4.582	0.641	0.254	0.702	0.269	3.527
42	1.000	0.0310	2.16	0.934	5627	0.785	4.497	0.373	4.655	0.641	0.254	0.702	0.269	3.766
43	1.000	0.0315	2.10	0.934	5595	0.768	4.497	0.388	4.444	0.641	0.263	0.700	0.270	3.749
44	1.000	0.0315	2.12	0.934	5604	0.773	4.497	0.383	4.520	0.640	0.262	0.701	0.270	3.500
45	1.000	0.0315	2.14	0.934	5612	0.777	4.497	0.377	4.595	0.640	0.262	0.701	0.270	3.519
46	1.000	0.0315	2.16	0.934	5620	0.782	4.497	0.372	4.669	0.639	0.261	0.701	0.269	3.890
47	1.000	0.0320	2.10	0.934	5589	0.764	4.497	0.387	4.457	0.641	0.271	0.699	0.271	3.659
48	1.000	0.0320	2.12	0.934	5598	0.769	4.497	0.382	4.535	0.640	0.270	0.700	0.270	3.444
49	1.000	0.0320	2.14	0.934	5606	0.774	4.497	0.376	4.609	0.639	0.269	0.700	0.270	3.609
50	1.000	0.0325	2.10	0.934	5584	0.762	4.497	0.386	4.477	0.640	0.278	0.698	0.271	3.564
51	1.000	0.0325	2.12	0.934	5592	0.766	4.497	0.380	4.555	0.639	0.277	0.698	0.271	3.505
52	1.000	0.0330	2.10	0.934	5578	0.759	4.497	0.384	4.498	0.640	0.285	0.697	0.272	3.493
53	1.000	0.0330	2.12	0.934	5587	0.763	4.497	0.379	4.574	0.640	0.285	0.697	0.272	3.580
54	1.000	0.0330	2.14	0.934	5595	0.768	4.497	0.373	4.650	0.638	0.284	0.698	0.271	3.887
55	1.000	0.0335	2.08	0.934	5564	0.751	4.497	0.389	4.438	0.640	0.293	0.696	0.273	3.742
56	1.000	0.0335	2.10	0.934	5573	0.756	4.497	0.383	4.518	0.639	0.292	0.696	0.273	3.692
57	1.000	0.0335	2.12	0.934	5581	0.760	4.497	0.377	4.595	0.638	0.292	0.696	0.272	3.753
58	1.000	0.0340	2.08	0.934	5559	0.748	4.497	0.387	4.459	0.639	0.300	0.695	0.273	3.631
59	1.000	0.0340	2.10	0.934	5567	0.753	4.497	0.381	4.538	0.639	0.300	0.695	0.273	3.737
60	1.000	0.0340	2.12	0.934	5576	0.757	4.497	0.376	4.615	0.638	0.299	0.695	0.273	3.727
61	1.000	0.0345	2.06	0.934	5545	0.741	4.497	0.392	4.398	0.639	0.308	0.693	0.274	3.957
62	1.000	0.0345	2.08	0.934	5553	0.745	4.497	0.386	4.480	0.639	0.307	0.694	0.274	3.720
63	1.000	0.0345	2.10	0.934	5562	0.750	4.497	0.380	4.558	0.638	0.307	0.694	0.274	3.692
64	1.000	0.0350	2.06	0.934	5539	0.738	4.497	0.390	4.418	0.639	0.315	0.692	0.275	3.922
65	1.000	0.0350	2.08	0.934	5548	0.742	4.497	0.384	4.499	0.638	0.314	0.692	0.275	3.731
66	1.000	0.0350	2.10	0.934	5557	0.747	4.497	0.378	4.579	0.639	0.313	0.693	0.274	3.761
67	1.000	0.0355	2.06	0.934	5534	0.735	4.497	0.389	4.439	0.639	0.322	0.691	0.276	3.779

No.	$M[M_{\odot}]$	Z_{init}	α_{MLT}	$R[R_{\odot}]$	T_{eff}	$L[L_{\odot}]$	$\log g$	X_{H}	$t_{\text{age}}[\text{Gyr}]$	$R_{\text{CZ}}[R_{\odot}]$	$[\text{Fe}/\text{H}]$	X_{s}	Y_{s}	χ_{CMM}^2
68	1.000	0.0355	2.08	0.934	5543	0.740	4.497	0.383	4.519	0.638	0.321	0.691	0.275	3.796
69	1.000	0.0355	2.10	0.934	5551	0.744	4.497	0.377	4.599	0.638	0.320	0.692	0.275	3.834
70	1.000	0.0360	2.06	0.934	5529	0.732	4.497	0.387	4.459	0.638	0.328	0.690	0.276	3.942
71	1.000	0.0360	2.08	0.934	5537	0.737	4.497	0.381	4.539	0.638	0.328	0.690	0.276	3.883
72	1.000	0.0365	2.06	0.934	5523	0.729	4.497	0.386	4.478	0.638	0.335	0.689	0.277	3.983
73	1.000	0.0370	2.06	0.934	5518	0.727	4.497	0.384	4.498	0.638	0.342	0.688	0.277	3.920
74	1.000	0.0375	2.04	0.934	5504	0.719	4.497	0.389	4.436	0.638	0.349	0.686	0.278	3.807
75	1.000	0.0375	2.06	0.934	5513	0.724	4.497	0.383	4.518	0.637	0.348	0.687	0.278	3.956
76	1.005	0.0300	2.14	0.935	5645	0.798	4.498	0.391	4.317	0.644	0.240	0.704	0.268	3.810
77	1.005	0.0300	2.16	0.935	5653	0.803	4.498	0.385	4.389	0.644	0.240	0.704	0.268	3.759
78	1.005	0.0300	2.18	0.935	5662	0.808	4.498	0.380	4.461	0.643	0.239	0.704	0.268	3.730
79	1.005	0.0305	2.14	0.935	5637	0.794	4.498	0.390	4.334	0.644	0.248	0.702	0.269	3.635
80	1.005	0.0305	2.16	0.935	5646	0.798	4.498	0.384	4.406	0.643	0.247	0.703	0.269	3.767
81	1.005	0.0305	2.18	0.935	5654	0.803	4.498	0.379	4.478	0.643	0.247	0.703	0.268	3.965
82	1.005	0.0310	2.12	0.935	5623	0.786	4.498	0.395	4.271	0.644	0.256	0.701	0.270	3.894
83	1.005	0.0310	2.14	0.935	5631	0.790	4.498	0.389	4.345	0.643	0.256	0.701	0.270	3.671
84	1.005	0.0310	2.16	0.935	5639	0.795	4.498	0.383	4.419	0.642	0.255	0.702	0.269	3.638
85	1.005	0.0315	2.12	0.935	5616	0.782	4.498	0.393	4.285	0.643	0.264	0.700	0.271	3.850
86	1.005	0.0315	2.14	0.935	5625	0.787	4.498	0.388	4.359	0.643	0.264	0.700	0.270	3.812
87	1.005	0.0315	2.16	0.935	5633	0.792	4.498	0.382	4.434	0.642	0.263	0.700	0.270	3.969
88	1.005	0.0320	2.14	0.935	5619	0.783	4.498	0.387	4.374	0.642	0.271	0.699	0.271	3.840
89	1.005	0.0325	2.12	0.935	5605	0.776	4.498	0.391	4.318	0.642	0.279	0.698	0.272	3.797
90	1.005	0.0335	2.12	0.935	5594	0.770	4.498	0.388	4.357	0.641	0.294	0.695	0.273	3.934

NOTE— The initial input parameters: stellar mass M , initial metal abundance Z_{init} , and mixing length parameter α_{MLT} are listed in column 2-4. The stellar parameters in column 5-14 present stellar radius R , effective temperature T_{eff} , luminosity L , surface gravity $\log g$, center hydrogen X_{H} , stellar age t_{age} , location of convection zone bottom R_{CZ} , $[\text{Fe}/\text{H}]$, surface hydrogen abundance X_{s} , and surface helium abundance Y_{s} , respectively. The last column presents the matching goodness χ_{CMM}^2 , which is calculated using Eq. (9). These results consider the effects of small-scale magnetic fields.

The distributions of χ_{CMM}^2 with stellar parameters for the models with $a = 570, b = 130$ are shown in Fig. 3. The filled circles represent the results of the better candidate models in Table 1. The panels (a)-(c) in Fig. 3 are the distributions of χ_{CMM}^2 with initial input parameters. The results show that as the stellar mass and mixing-length parameter α_{MLT} increase, χ_{CMM}^2 decreased, reaching a minimum at $M = 1.0M_{\odot}$ and $\alpha_{\text{MLT}} = 2.12$, respectively, before gradually increasing again. According to these results, the mixing-length parameter $\alpha = 2.12$ for KIC 8006161 is greater than that of the standard solar model. In general, for solar-like stars, the larger the convective mixing length parameter, the higher the convection energy transfer efficiency, which results in a higher effective temperature. This star has a smaller stellar radius. From panel (b), χ_{CMM}^2 is insensitive to the initial metal abundance Z_{init} . Z_{init} for the better candidate models in Table 1 occupies a wide range in parameter space.

The panels (d)-(i) in Fig. 3 show the distributions of χ_{CMM}^2 with stellar parameters. We find that the distributions of χ_{CMM}^2 with stellar parameters converge to narrow ranges. It is very useful to accurately determine these stellar parameters. From panel (d), for KIC 8006161, the stellar radius is about $0.934R_{\odot}$, which is smaller than the solar radius. This result corresponds to larger mixing length parameter. On the other hand, the scaling relation for the large-frequency separation $\Delta\nu$ from Kjeldsen & Bedding (1995) is: $\Delta\nu/\Delta\nu_{\odot} \approx (M/M_{\odot})^{1/2}(R/R_{\odot})^{-3/2}$. For a solar-like star with $1M_{\odot}$, the stellar radius is inversely proportional to the large-frequency separation. The large-frequency separation of KIC 8006161 is about $149.4\mu\text{Hz}$ (Lund et al. 2017), which is greater than that of the sun with $134.9\mu\text{Hz}$. KIC 8006161 has a smaller stellar radius. From this figure, we can get that KIC 8006161 is a main sequence star with a convective envelope covering $0.315R$. The stellar central hydrogen mass fraction is about 0.382, and the stellar age is about 4.53 Gyr.

In the calculations above, we use the chemical enrichment law $\Delta Y/\Delta Z = 1.33$ (Li et al. 2018) to determine the initial helium abundance. Silva Aguirre et al. (2017) used seven independent pipelines to determine the stellar properties of

Table 2. Comparison between the parameters of theoretical models and spectroscopic parameters.

Parameters	Creevey et al. (2017)	Silva Aguirre et al. (2017)	Our results $Y_{\text{init}} = 0.249 + 1.33Z_{\text{init}}$	Our results Y_{init} as a parameter	Spectroscopic parameters (Buchhave & Latham 2015)
$M/(M_{\odot})$	1.000 ± 0.030	0.9861 ± 0.0253	$1.000^{+0.005}_{-0.010}$	$1.02^{+0.02}_{-0.03}$	
R/R_{\odot}	0.930 ± 0.009	0.9293 ± 0.0083	$0.934^{+0.001}_{-0.003}$	$0.940^{+0.007}_{-0.009}$	
L/L_{\odot}	0.64 ± 0.03	0.7001 ± 0.0473	$0.769^{+0.039}_{-0.078}$	$0.656^{+0.163}_{-0.097}$	
T_{eff}/K	5351 ± 49		5598^{+64}_{-143}	5361^{+320}_{-211}	5488 ± 77
$\log g$	4.498 ± 0.003	4.4953 ± 0.0034	$4.497^{+0.001}_{-0.001}$	$4.500^{+0.003}_{-0.004}$	
$t_{\text{age}}(Gy)$	4.57 ± 0.36	5.1012 ± 0.3253	$4.53^{+0.30}_{-0.26}$	$4.90^{+0.79}_{-0.63}$	
[Fe/H]	0.41 ± 0.04		$0.270^{+0.103}_{-0.032}$	$0.325^{+0.062}_{-0.120}$	0.34 ± 0.08
R_{Cz}/R		0.6927 ± 0.0037	$0.685^{+0.004}_{-0.005}$	$0.679^{+0.012}_{-0.005}$	
X_C		0.3979 ± 0.0260	$0.382^{+0.013}_{-0.014}$	$0.423^{+0.041}_{-0.057}$	

66 main-sequence targets. The four pipelines presented the distribution of initial helium abundance and initial metal abundance for all targets. However, the slopes of the function relating initial helium abundance and initial metal abundance differ among them. Verma et al. (2019) used the measured surface abundances in combination with the settling predicted by the stellar models to obtain a Galactic enrichment ratio of $\Delta Y/\Delta Z = 1.226 \pm 0.849$. In our work, we also consider models with initial helium abundance as a free parameter for $a = 570$ and $b = 130$. We set the initial helium abundance Y_{init} to range from 0.26 to 0.32, in steps of 0.005. The stellar mass M varies from 0.98 to $1.04 M_{\odot}$ with a step of $0.01 M_{\odot}$. The ranges for the other parameters remain unchanged from the previous calculations.

After calculating the stellar structure and evolution of all the models, we obtain the best-fit model with a minimum χ^2_{CMM} of 2.68. The corresponding parameters are $M = 1.02 M_{\odot}$, $Y_{\text{init}} = 0.270$, $Z_{\text{init}} = 0.037$, and $\alpha = 1.98$. Compared to the results from models with $Y_{\text{init}} = 0.249 + 1.33Z_{\text{init}}$, the best-fit model with the initial helium abundance as a free parameter has a lower χ^2_{CMM} and a larger stellar mass. The initial helium abundance Y_{init} for the best-fit model, where Y_{init} is treated as a free parameter, is lower than the value obtained using the relation $Y_{\text{init}} = 0.249 + 1.33Z_{\text{init}}$. This result is very similar to those from Silva Aguirre et al. (2017).

For comparison, the stellar parameters of our theoretical models and those obtained from the literatures (Creevey et al. 2017, Silva Aguirre et al. 2017) for KIC 8006161 are all listed in Table 2. The basic parameters of Creevey et al. (2017) were generated by the latest version of Asteroseismic Modeling Portal (AMP). Silva Aguirre et al. (2017) used seven codes by the different teams to calculate the stellar properties. We find that the stellar mass from Creevey et al. (2017) is in complete agreement with the one we obtain using $Y_{\text{init}} = 0.249 + 1.33Z_{\text{init}}$. In contrast, the stellar mass from Silva Aguirre et al. (2017) is smaller, while the models where Y_{init} is treated as a free parameter yield the highest mass. The values of other stellar parameters (i.e. R , $\log g$, R_{Cz}/R , X_C) show a high degree of similarity, with some overlap. Due to the smaller stellar masses reported by Silva Aguirre et al. (2017), the corresponding stellar ages are larger. Compared to the Gaia data for KIC 8006161 which has a luminosity of $0.680 L_{\odot}$ (Gaia Collaboration et al. 2018), all models except our results with $Y_{\text{init}} = 0.249 + 1.33Z_{\text{init}}$ are consistent with the observed data. Due to the lower metallicity of our models with $Y_{\text{init}} = 0.249 + 1.33Z_{\text{init}}$, the stellar luminosity and effective temperature are larger than those from other models. However, all of them overlap with the results of spectral parameters: $T_{\text{eff}} = 5488 \pm 77$ K, $[\text{Fe}/\text{H}] = 0.34 \pm 0.08$ (Buchhave & Latham 2015, Karoff et al. 2018).

In order to show the matching details, we present the Échelle diagram of observation and the best-fit model with different Y_{init} and the corresponding ratio r_{ij} of small to large-frequency separations in Fig. 4. The filled gray points represent the observed data, while the open red and blue points show the results of best-fit model with $Y_{\text{init}} = 0.249 + 1.33Z_{\text{init}}$ and Y_{init} as a free parameter for $a = 570$, and $b = 130$, respectively. From Fig. 4, it can be seen that whether Y_{init} is set to $0.249 + 1.33Z_{\text{init}}$ or treated as a free parameter, the Échelle diagram and corresponding frequency ratios of the best-fit models are essentially identical. In the left panel, except for a few higher frequencies for $l = 0, l = 1$, the most frequencies for the best-fit model with magnetic fields are in good agreement with the observation. In the right panel of Fig. 4, we present the distribution of ratios r_{ij} with frequencies. The errors of the frequency ratios in the observations are obtained from Lund et al. (2017), and the theoretical ratios are calculated using Eq. (2) and (3). We find that for higher frequencies, the differences in the frequency ratios between the best-fit

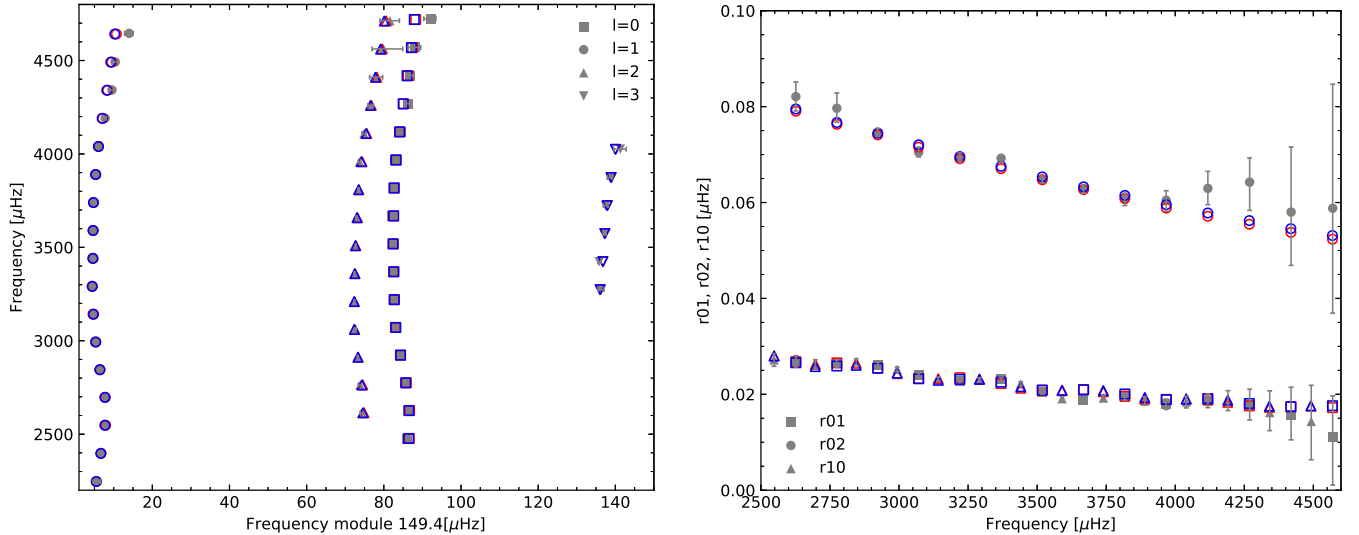


Figure 4. The Échelle diagram of observation data (filled gray points) of KIC 8006161 and the best-fit model with $Y_{\text{init}} = 0.249 + 1.33Z_{\text{init}}$ (open red points) and Y_{init} as a free parameter (open blue points) and the corresponding ratio r_{ij} of small to large-frequency separations for $a = 570$, and $b = 130$. The errors of the observed frequencies and frequency ratios are from Lund et al. (2017). The theoretical frequencies only consider the effects of small-scale magnetic fields, and do not include other physics associated with near-surface effects (i.e. Ball et al. 2016, Houdek et al. 2017, Schou & Birch 2020).

model with Y_{init} as $0.249 + 1.33Z_{\text{init}}$ and as a free parameter and the observed data are larger. But due to the large errors in high-frequency observations, the majority of the theoretical ratio r_{ij} are within the observed error range.

It is worth noting that these results do not take into account the other physics associated with near-surface effects. Comparing the observed oscillation frequencies with the theoretical ones, Christensen-Dalsgaard et al. (1988) found a systematical offset between them for the Sun. This offset was independent of the spherical degree ℓ , but it increased with frequency (Christensen-Dalsgaard et al. 1988; Dziembowski et al. 1988). This is known as the near-surface effect of solar p-mode oscillation.

In general, the near-surface effect is mainly due to the interactions between p-mode oscillations and turbulent convection near the top of the stellar convection zone. Rosenthal et al. (1999) considered the averages of hydrodynamical simulations and found that turbulent pressure provided additional support against gravity. This would result in higher turning points of high-frequency modes. Subsequently, Ball et al. (2016) used averaged three-dimensional radiation hydrodynamics simulation (Beeck et al. 2013) to replace the near-surface structure of dwarfs with different spectral types. Houdek et al. considered the averaged structure of a 3D hydrodynamical simulation and the physical effects of non-adiabaticity and turbulent pressure (Houdek et al. 2017; Schou & Birch 2020; Jørgensen et al. 2021). They got the frequency deviations with $\leq 3\mu\text{Hz}$ for the sun. In this work, we only consider the influence of small-scale magnetic fields on the oscillation frequencies of solar-like star KIC 8006161 and do not include the effects of non-adiabaticity and turbulent pressure.

3.2. Small-scale magnetic fields

The magnetic fields and the acoustic waves are coupled with each other. Fig. 5 presents the distributions of gas pressure and magnetic pressure with height for the best-fit model with $Y_{\text{init}} = 0.249 + 1.33Z_{\text{init}}$ (red lines) and Y_{init} as a free parameter (blue lines). When the stellar magnetic pressure increases with height, the gas pressure decreases. This subsequently leads to a decrease in density and an increase in acoustic speed. According to Rosenthal et al. (2002) and Cally (2007), the acoustic waves are reflected and transmitted at a position where the gas pressure equals magnetic pressure. We use this condition to calculate the magnetic field strength and determine the location of the magnetic-arch splicing layer for the best-fit model with $Y_{\text{init}} = 0.249 + 1.33Z_{\text{init}}$ and Y_{init} as a free parameter. We find that the magnetic field strength for the best-fit model with $Y_{\text{init}} = 0.249 + 1.33Z_{\text{init}}$ is 96 G, and the height of

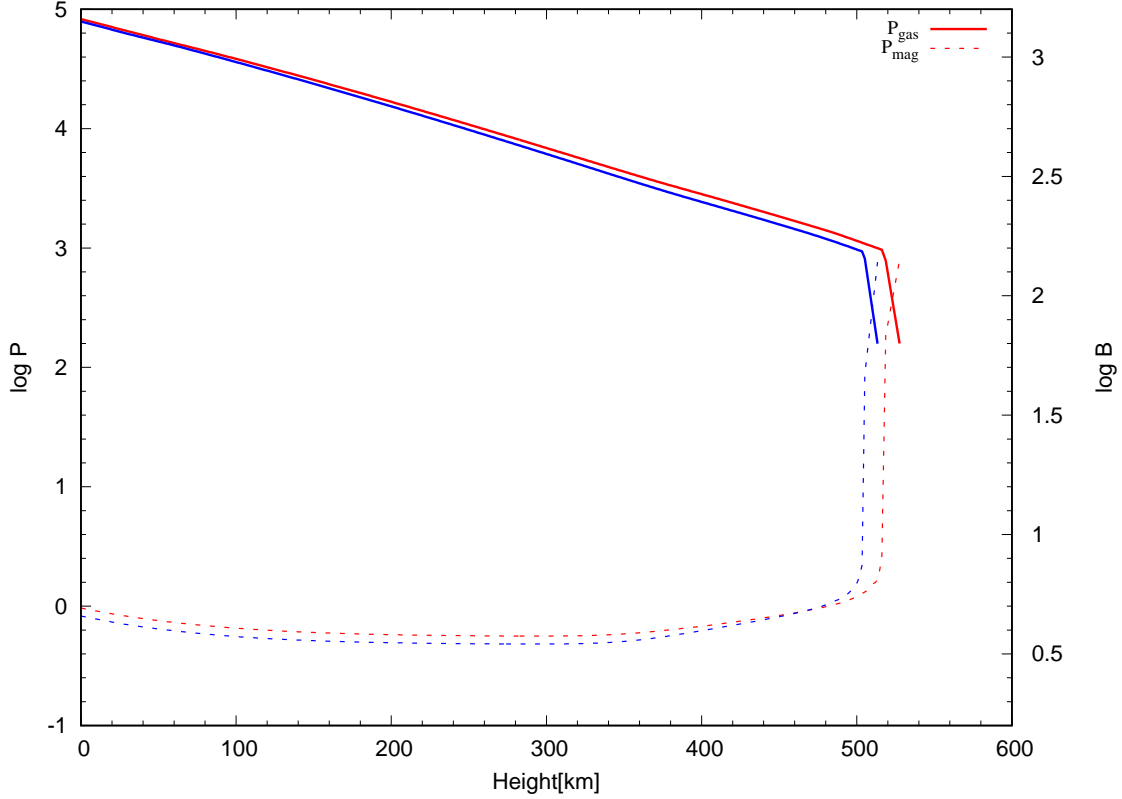


Figure 5. The distributions of the gas pressure and the magnetic pressure, as well as the fields strength for the best-fit model with $Y_{\text{init}} = 0.249 + 1.33Z_{\text{init}}$ (red lines) and Y_{init} as a free parameter (blue lines) by adopting the grey atmosphere.

the magnetic-arch splicing layer is 522 km. For the best-fit model with Y_{init} as a free parameter, the magnetic field strength is 89 G, and the height of the splicing layer is about 510 km. This result also indicates that whether Y_{init} is varied with $\Delta Y/\Delta Z$ or treated as a free parameter, the best-fit model has a similar stellar small-scale magnetic field strength. In addition, there is a large area below the magnetic-arch splicing layer in Fig. 5 with a very low magnetic field strength. This is very similar to the configuration of magnetic voids just below the arches observed in the magneto-hydrodynamic (MHD) simulations (Schaffenberger et al. 2005, 2006).

KIC 8006161 is a main sequence star with a higher metallicity. Table 2 presents the stellar parameters for KIC 8006161. We can get that KIC 8006161 is a star with $\sim 1M_{\odot}$ and a smaller stellar radius. The stellar age is similar to that of the sun. Although the origin mechanism of small-scale magnetic fields is still controversial, stellar convection plays an important role in their generation. We compare the distribution of stellar physical properties in the convection zone between KIC 8006161 and the sun.

We use the results of the solar model from Li et al. (2021), and present a comparison of the typical velocity of turbulent motions between two stars in the left panel of Fig. 6. The black dotted line represents the result of the solar model, while the red and blue lines represent the results of a best-fit model with $Y_{\text{init}} = 0.249 + 1.33Z_{\text{init}}$ and Y_{init} as a free parameter, respectively. It can be seen that KIC 8006161 has a deeper convection zone. The best-fit model with $Y_{\text{init}} = 0.249 + 1.33Z_{\text{init}}$ and the solar model have nearly identical maximum turbulence velocities (about $2.6 \times 10^5 \text{ cm s}^{-1}$), while the best-fit model with Y_{init} as a free parameter exhibits slightly lower maximum turbulence velocities (about $2.4 \times 10^5 \text{ cm s}^{-1}$). Except for the different location of convection zone bottom, the distribution of typical velocity of turbulent motions is basically the same for the solar model and the best-fit model with $Y_{\text{init}} = 0.249 + 1.33Z_{\text{init}}$. We also compare the typical size of convective rolling cells in the right panel of Fig. 6, which is expressed by Eq. (58) from Li (2012). We can get that the typical size of convective rolling cells R_b in a $k-w$ model (Li 2012) is nearly consistent with each other just below the stellar photosphere. On the stellar surface, convective rolling cells can reach scales of more than one thousand kilometers.

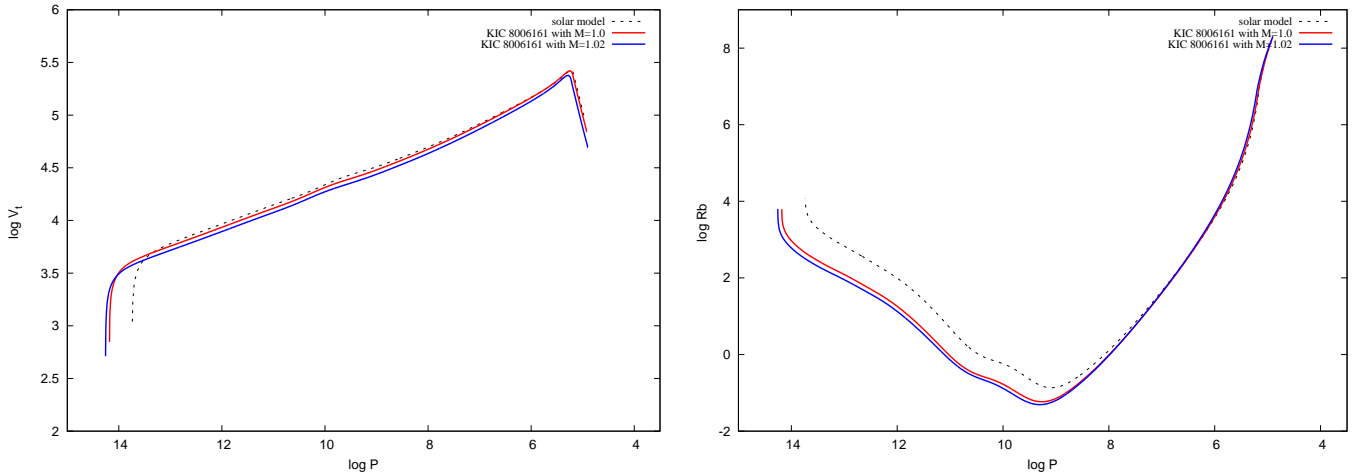


Figure 6. The distribution of physical quantities in the convection zone between KIC 8006161 (solid lines) and the solar model (dashed lines) from Li et al. (2021). The red lines represent the results of the best-fit model with $Y_{\text{init}} = 0.249 + 1.33Z_{\text{init}}$, and the blue lines represent the results of the best-fit model with Y_{init} treated as a free parameter. The left panel is the distribution of typical velocity of turbulent motions with $\log P$ in the convection zone. The right panel is the distribution of typical size of convective rolling cells.

In summary, although there are some differences in the fundamental parameters between KIC 8006161 and the solar model, the characteristics of the convection zone (i.e. maximum velocity of turbulence and typical size of convective rolling cells) are very similar to each other. Our theoretical model suggests that the small-scale magnetic field strength of KIC 8006161 is very similar to that of the sun.

4. SUMMARY

For solar-like stars, there is a convective envelope on the stellar surface. The small-scale magnetic fields may be widely distributed on the surface of solar-like stars. Because small-scale magnetic fields are ubiquitous on stellar surface (Li et al. 2021; Trujillo Bueno et al. 2004), they store a amount of magnetic energy. This would affect the heating of the corona and the acceleration of the stellar wind (Stenflo 1994; Schrijver et al. 1998; Schrijver & Title 2003). In addition, the small-scale magnetic fields are coupled with the acoustic wave, influencing the propagation speed of the wave (Rosenthal et al. 2002; Bogdan et al. 2003; Cally 2007). This also provides us with an opportunity to use asteroseismology to constrain the small-scale magnetic field of solar-like star.

In this work, considering the effects of small-scale magnetic fields in the photosphere on the oscillation frequencies, we attempt to use the observed oscillation frequencies to constrain the stellar fundamental parameters for KIC 8006161, and especially get the strength of the small-scale magnetic fields. In our model, we assume that the surface effects are caused by the small-scale magnetic fields of the star. We approximate the influence of the magnetic field by incorporating magnetic pressure into the grey-atmosphere model. Due to the impact of turbulent pressure, which provides additional support against gravity (Rosenthal et al. 1999; Houdek et al. 2017; Schou & Birch 2020; Jørgensen et al. 2021), the magnetic field strength obtained from our models may approach the upper limit of KIC 8006161. Our main conclusions are as follows:

1. Considering the effects of small-scale magnetic fields in the photosphere, we derived the stellar fundamental parameters with a χ^2 -minimum method of iterative computation for KIC 8006161, which are listed in Table 2. We use two methods to determine the initial helium abundance Y_{init} : one uses the chemical enrichment law $\Delta Y/\Delta Z = 1.33$, and the other treats Y_{init} as a free parameter. We find that considering the effects of small-scale magnetic fields in the photosphere, the stellar fundamental parameters obtained by two methods are consistent with the results from spectroscopic observations. In addition, the initial helium abundance Y_{init} for the best-fit model with Y_{init} as a free parameter is lower than the value obtained from the relation $Y_{\text{init}} = 0.249 + 1.33Z_{\text{init}}$. The corresponding stellar mass is also larger, $\sim 1.02M_{\odot}$. The other fundamental parameters (i.e. radius R , $\log g$, R_{CZ}/R , X_{C}) are completely consistent for both models.

2. Considering the effects of small-scale magnetic fields regardless of the value of Y_{init} , most of the theoretical frequencies are in agreement with the observational ones. Meanwhile, most of the ratio r_{ij} of small to large-frequency separations for the best-fit model with $Y_{\text{init}} = 0.249 + 1.33Z_{\text{init}}$ and Y_{init} as a free parameter also agree with the observational ones. This also implies that our best-fit model is in good agreement with observations from the star's interior to its surface.

3. The small-scale magnetic field strength for KIC 8006161, independently derived from our model with $Y_{\text{init}} = 0.249 + 1.33Z_{\text{init}}$ and Y_{init} as a free parameter, is approximately 96 G and 89 G, respectively. The corresponding locations of the magnetic-arch splicing layer are about 522 km and 510 km, respectively. Since the stellar convective properties for KIC 8006161 are similar to those of the solar model from Li et al. (2021), regardless of the value of Y_{init} , the magnetic field strength is also similar to that of the sun.

This research is supported by National Natural Science Foundation of China (grant No. 12288102 and 12133011), National Key R&D Program of China (grant No. 2021YFA1600400/2021YFA1600402), the B-type Strategic Priority Program of Chinese Academy of Sciences (grant No. XDB41000000), National Natural Science Foundation of China (grant No. 12273104), Yunnan Fundamental Research Projects (grant No. 202401AS070045), International Center of Supernovae at the Yunnan Key Laboratory (grant No. 202302AN360001/202302AN36000101) and the West Light Foundation of the Chinese Academy of Sciences. T. W. thanks for financial support from Youth Innovation Promotion Association of Chinese Academy of Sciences, and Yunnan Ten Thousand Talents Plan Young & Elite Talents Project.

REFERENCES

- Abbett, W. P. 2007, *ApJ*, 665, 1469, doi: [10.1086/519788](https://doi.org/10.1086/519788)
- Ball, W. H., Beeck, B., Cameron, R. H., & Gizon, L. 2016, *A&A*, 592, A159, doi: [10.1051/0004-6361/201628300](https://doi.org/10.1051/0004-6361/201628300)
- Beeck, B., Cameron, R. H., Reiners, A., & Schüssler, M. 2013, *A&A*, 558, A48, doi: [10.1051/0004-6361/201321343](https://doi.org/10.1051/0004-6361/201321343)
- Bogdan, T. J., Carlsson, M., Hansteen, V. H., et al. 2003, *ApJ*, 599, 626, doi: [10.1086/378512](https://doi.org/10.1086/378512)
- Böhm-Vitense, E. 1958, *ZA*, 46, 108
- Buchhave, L. A., & Latham, D. W. 2015, *ApJ*, 808, 187, doi: [10.1088/0004-637X/808/2/187](https://doi.org/10.1088/0004-637X/808/2/187)
- Cally, P. S. 2007, *Astronomische Nachrichten*, 328, 286, doi: [10.1002/asna.200610731](https://doi.org/10.1002/asna.200610731)
- Cattaneo, F. 1999, *ApJL*, 515, L39, doi: [10.1086/311962](https://doi.org/10.1086/311962)
- Christensen-Dalsgaard, J. 2008, *Ap&SS*, 316, 113, doi: [10.1007/s10509-007-9689-z](https://doi.org/10.1007/s10509-007-9689-z)
- Christensen-Dalsgaard, J., Dappen, W., & Lebreton, Y. 1988, *Nature*, 336, 634, doi: [10.1038/336634a0](https://doi.org/10.1038/336634a0)
- Creevey, O. L., Metcalfe, T. S., Schultheis, M., et al. 2017, *A&A*, 601, A67, doi: [10.1051/0004-6361/201629496](https://doi.org/10.1051/0004-6361/201629496)
- Danilovic, S., Beeck, B., Pietarila, A., et al. 2010, *ApJL*, 723, L149, doi: [10.1088/2041-8205/723/2/L149](https://doi.org/10.1088/2041-8205/723/2/L149)
- Deheuvels, S., Li, G., Ballot, J., & Lignières, F. 2023, *A&A*, 670, L16, doi: [10.1051/0004-6361/202245282](https://doi.org/10.1051/0004-6361/202245282)
- Dziembowski, W. A., Paterno, L., & Ventura, R. 1988, *A&A*, 200, 213
- Eggenberger, P., Charbonnel, C., Talon, S., et al. 2004, *A&A*, 417, 235, doi: [10.1051/0004-6361:20034203](https://doi.org/10.1051/0004-6361:20034203)
- Gaia Collaboration, Brown, A. G. A., Vallenari, A., et al. 2018, *A&A*, 616, A1, doi: [10.1051/0004-6361/201833051](https://doi.org/10.1051/0004-6361/201833051)
- Gough, D. O., & Thompson, M. J. 1990, *MNRAS*, 242, 25, doi: [10.1093/mnras/242.1.25](https://doi.org/10.1093/mnras/242.1.25)
- Grevesse, N., & Sauval, A. J. 1998, *SSRv*, 85, 161, doi: [10.1023/A:1005161325181](https://doi.org/10.1023/A:1005161325181)
- Houdek, G., Trampedach, R., Aarslev, M. J., & Christensen-Dalsgaard, J. 2017, *MNRAS*, 464, L124, doi: [10.1093/mnrasl/slw193](https://doi.org/10.1093/mnrasl/slw193)
- Iglesias, C. A., & Rogers, F. J. 1996, *ApJ*, 464, 943, doi: [10.1086/177381](https://doi.org/10.1086/177381)
- Jin, C. L., & Wang, J. X. 2015, *ApJ*, 807, 70, doi: [10.1088/0004-637X/807/1/70](https://doi.org/10.1088/0004-637X/807/1/70)
- Jørgensen, A. C. S., Montalbán, J., Angelou, G. C., et al. 2021, *MNRAS*, 500, 4277, doi: [10.1093/mnras/staa3476](https://doi.org/10.1093/mnras/staa3476)
- Karoff, C., Metcalfe, T. S., Santos, Â. R. G., et al. 2018, *ApJ*, 852, 46, doi: [10.3847/1538-4357/aaa026](https://doi.org/10.3847/1538-4357/aaa026)
- Kjeldsen, H., & Bedding, T. R. 1995, *A&A*, 293, 87, doi: [10.48550/arXiv.astro-ph/9403015](https://doi.org/10.48550/arXiv.astro-ph/9403015)
- Li, G., Deheuvels, S., Ballot, J., & Lignières, F. 2022, *Nature*, 610, 43, doi: [10.1038/s41586-022-05176-0](https://doi.org/10.1038/s41586-022-05176-0)
- Li, T., Bedding, T. R., Huber, D., et al. 2018, *MNRAS*, 475, 981, doi: [10.1093/mnras/stx3079](https://doi.org/10.1093/mnras/stx3079)
- Li, Y. 2012, *ApJ*, 756, 37, doi: [10.1088/0004-637X/756/1/37](https://doi.org/10.1088/0004-637X/756/1/37)
- Li, Y., Zhang, Q.-s., Wu, T., et al. 2021, *ApJ*, 916, 107, doi: [10.3847/1538-4357/ac0882](https://doi.org/10.3847/1538-4357/ac0882)
- Lites, B. W., Leka, K. D., Skumanich, A., Martinez Pillet, V., & Shimizu, T. 1996, *ApJ*, 460, 1019, doi: [10.1086/177028](https://doi.org/10.1086/177028)

- Lites, B. W., Rempel, M., Borrero, J. M., & Danilovic, S. 2017, *ApJ*, 835, 14, doi: [10.3847/1538-4357/835/1/14](https://doi.org/10.3847/1538-4357/835/1/14)
- Lites, B. W., Kubo, M., Socas-Navarro, H., et al. 2008, *ApJ*, 672, 1237, doi: [10.1086/522922](https://doi.org/10.1086/522922)
- Lund, M. N., Silva Aguirre, V., Davies, G. R., et al. 2017, *ApJ*, 850, 110, doi: [10.3847/1538-4357/aa9658](https://doi.org/10.3847/1538-4357/aa9658)
- Martínez González, M. J., Pastor Yabar, A., Lagg, A., et al. 2016, *A&A*, 596, A5, doi: [10.1051/0004-6361/201628449](https://doi.org/10.1051/0004-6361/201628449)
- Morel, P., & Thévenin, F. 2002, *A&A*, 390, 611, doi: [10.1051/0004-6361:20020768](https://doi.org/10.1051/0004-6361:20020768)
- Morosin, R., de la Cruz Rodríguez, J., Vissers, G. J. M., & Yadav, R. 2020, *A&A*, 642, A210, doi: [10.1051/0004-6361/202038754](https://doi.org/10.1051/0004-6361/202038754)
- Paxton, B., Bildsten, L., Dotter, A., et al. 2011, *ApJS*, 192, 3, doi: [10.1088/0067-0049/192/1/3](https://doi.org/10.1088/0067-0049/192/1/3)
- Paxton, B., Schwab, J., Bauer, E. B., et al. 2018, *ApJS*, 234, 34, doi: [10.3847/1538-4365/aaa5a8](https://doi.org/10.3847/1538-4365/aaa5a8)
- Rempel, M. 2014, *ApJ*, 789, 132, doi: [10.1088/0004-637X/789/2/132](https://doi.org/10.1088/0004-637X/789/2/132)
- Rogers, F. J., & Nayfonov, A. 2002, *ApJ*, 576, 1064, doi: [10.1086/341894](https://doi.org/10.1086/341894)
- Rosenthal, C. S., Christensen-Dalsgaard, J., Nordlund, Å., Stein, R. F., & Trampedach, R. 1999, *A&A*, 351, 689, doi: [10.48550/arXiv.astro-ph/9803206](https://doi.org/10.48550/arXiv.astro-ph/9803206)
- Rosenthal, C. S., Bogdan, T. J., Carlsson, M., et al. 2002, *ApJ*, 564, 508, doi: [10.1086/324214](https://doi.org/10.1086/324214)
- Roxburgh, I. W., & Vorontsov, S. V. 2003, *A&A*, 411, 215, doi: [10.1051/0004-6361:20031318](https://doi.org/10.1051/0004-6361:20031318)
- Schaffnerberger, W., Wedemeyer-Böhm, S., Steiner, O., & Freytag, B. 2005, in *ESA Special Publication*, Vol. 596, *Chromospheric and Coronal Magnetic Fields*, ed. D. E. Innes, A. Lagg, & S. A. Solanki, 65.1
- Schaffnerberger, W., Wedemeyer-Böhm, S., Steiner, O., & Freytag, B. 2006, in *Astronomical Society of the Pacific Conference Series*, Vol. 354, *Solar MHD Theory and Observations: A High Spatial Resolution Perspective*, ed. J. Leibacher, R. F. Stein, & H. Uitenbroek, 345
- Schou, J., & Birch, A. C. 2020, *A&A*, 638, A51, doi: [10.1051/0004-6361/201936530](https://doi.org/10.1051/0004-6361/201936530)
- Schrijver, C. J., & Title, A. M. 2003, *ApJL*, 597, L165, doi: [10.1086/379870](https://doi.org/10.1086/379870)
- Schrijver, C. J., Title, A. M., Harvey, K. L., et al. 1998, *Nature*, 394, 152, doi: [10.1038/28108](https://doi.org/10.1038/28108)
- Schüssler, M., & Vögler, A. 2008, *A&A*, 481, L5, doi: [10.1051/0004-6361:20078998](https://doi.org/10.1051/0004-6361:20078998)
- Silva Aguirre, V., Lund, M. N., Antia, H. M., et al. 2017, *ApJ*, 835, 173, doi: [10.3847/1538-4357/835/2/173](https://doi.org/10.3847/1538-4357/835/2/173)
- Steiner, O., Rezaei, R., Schaffnerberger, W., & Wedemeyer-Böhm, S. 2008, *ApJL*, 680, L85, doi: [10.1086/589740](https://doi.org/10.1086/589740)
- Stenflo, J. 1994, *Solar Magnetic Fields: Polarized Radiation Diagnostics*, Vol. 189, doi: [10.1007/978-94-015-8246-9](https://doi.org/10.1007/978-94-015-8246-9)
- Trujillo Bueno, J., Shchukina, N., & Asensio Ramos, A. 2004, *Nature*, 430, 326, doi: [10.1038/nature02669](https://doi.org/10.1038/nature02669)
- Verma, K., Raodeo, K., Basu, S., et al. 2019, *MNRAS*, 483, 4678, doi: [10.1093/mnras/sty3374](https://doi.org/10.1093/mnras/sty3374)
- Wu, T., & Li, Y. 2016, *ApJL*, 818, L13, doi: [10.3847/2041-8205/818/1/L13](https://doi.org/10.3847/2041-8205/818/1/L13)